Improved high-fidelity transport of trapped-ion qubits through a multi-dimensional array

R.B. Blakestad,[*] C. Ospelkaus,[†] A.P. VanDevender,[‡]

J.H. Wesenberg,[§] M.J. Biercuk,[¶] D. Leibfried, and D.J. Wineland

National Institute of Standards and Technology, 325 Broadway, Boulder, Colorado 80305, USA

(Dated: June 27, 2011)

We have demonstrated transport of $^9\mathrm{Be}^+$ ions through a 2D Paul-trap array that incorporates an X-junction, while maintaining the ions near the motional ground-state of the confining potential well. We expand on the first report of the experiment [1], including a detailed discussion of how the transport potentials were calculated. Two main mechanisms that caused motional excitation during transport are explained, along with the methods used to mitigate such excitation. We reduced the motional excitation below the results in Ref. [1] by a factor of approximately 50. The effect of a mu-metal shield on qubit coherence is also reported. Finally, we examined a method for exchanging energy between multiple motional modes on the few-quanta level, which could be useful for cooling motional modes without directly accessing the modes with lasers. These results establish how trapped ions can be transported in a large-scale quantum processor with high fidelity.

I. INTRODUCTION

The reliable transport of quantum information will enable operations between any arbitrarily selected qubits in a quantum processor and is essential to realize efficient, large-scale quantum information processing (QIP). Trapped ions are a promising system in which to study QIP [2–4], and several approaches to achieving reliable information transport have been proposed [2–9]. In most demonstrated entangling gate operations that use ions, qubits stored in the internal atomic states of ions are entangled by coupling the internal states with a single shared motional mode through a laser-induced interaction [2–4, 10]. However, as the number of ions grows large (> 10), it becomes difficult to isolate a single mode during gate operations [6, 11]. One way around this issue is to distribute the ions over an array of harmonic potentials, where the number of ions in each trapping potential can remain small. The potentials can be adjusted temporally to transport the ions throughout the array and combine selected ions into a particular harmonic potential. Once combined, gate operations can be performed on the selected ions by use of a local shared mode of motion [6, 7].

Initial demonstrations of such distributed architectures have incorporated simple linear arrays [12–16], where all ions are confined in potential minima on a line along an axis of the trap. The order of ions within the linear array can even be changed [17]. However, multidimensional arrays [6, 7] provide the greatest flexibility in ion-trap processor architectures, and permit more efficient reordering of ion strings for deterministic gate operations. The key technical element that must be realized towards this end is the two-dimensional junction, which consists of multiple intersecting linear arrays. The potentials in a junction are more complicated than those in a linear array, making transport through a junction challenging. Since the fidelity of the gates is highest if the ions are near their motional ground state, it is important that transport through such arrays be performed reliably and with minimal excitation of the ion's motion in its local trapping potential. If multiple transports are needed, each transport should contribute well under a single quantum of motional excitation, though sympathetic cooling can be used to remove excess motional energy, at the cost of increased experiment duration (and accompanying decoherence) [7]. For simple linear arrays, reliable transport with little motional excitation has been demonstrated [12, 13, 15].

To date, transport through a T-junction [18], an X-junction [1] and surface-electrode Y-junctions [19, 20] have been demonstrated. However, such transport has not yet been demonstrated with sufficiently-low motional excitation (at or below a single quantum). Using the apparatus in Ref. [1], we have now realized highly reliable transport through an X-junction with excitation of less than one quantum of motion per transport, a decrease of approximately 50 compared to the results in Ref. [1]. This has allowed us to observe a process where energy can be exchanged between motional modes in certain situations, and demonstrates motional control over the ions at the single-quantum level. The paper is organized as follows: we begin in Sec. II with a description of the X-junction trap array used for transport. Sec-

---

[*]Present address: Joint Quantum Institute, NIST and University of Maryland, Gaithersburg, MD 20899, USA

[†]Present address: QUEST, Leibniz Universität Hannover, 30167 Hannover and PTB, 38116 Braunschweig, Germany

[‡]Present address: Halcyon Molecular, Redwood City, CA 94063, USA

[§]Present address: Centre for Quantum Technologies, National University of Singapore, Singapore 117543, Singapore

[¶]Present address: School of Physics, The University of Sydney, NSW 2006 Australia.

tion III lays out the procedure for calculating the time-dependent trapping potentials that transport the ion. A description of the basic transport experiment is given in Sec. IV. Section V covers the various mechanisms that excite the ion's motion during transport, as well as the filtering techniques used to mitigate those excitations. This understanding of the noise sources, and the subsequent improved filtering techniques, allowed the reduction in motional excitation relative to Ref. [1]. To mitigate the effects of magnetic field fluctuations on qubit decoherence, a mu-metal shield and field-coil current stabilization were used, which is explained in Sec. VI. Finally, in Sec. VII, we discuss a procedure for swapping motional energy between motional modes at the center of the junction array. This swapping process can potentially be used to laser-cool multiple modes of motion without the need for a direct interaction between the cooling laser and every motional mode.

II. X-JUNCTION ARRAY

The X-junction array was based on the design of previous two-layer linear RF Paul traps [12, 13, 21]. The current trap consisted of a stack of five high-purity alumina (99.6% Al_2O_3) wafers clamped together (Fig. 1) with screws (visible in Fig. 2). The trap electrodes resided in the 'top' and 'bottom' wafers. These wafers (125 μm thick) were laser machined to cut out 'main channels' through the wafers, with opposite sides of the channel forming rf and control electrodes. Slits, nominally perpendicular to the main channel axes, separated the control electrode side of the channel into a series of cantilevered structures to produce separate control electrodes. Electrodes were formed onto the Al_2O_3 by evaporating through a shadow-mask a 30 nm titanium adhesion layer followed by 0.5 μm of gold, then overcoating with 3 μm of electroplated gold. Care was taken to coat all sides of each cantilevered structure to minimize exposed dielectric that could otherwise charge and shift the potential minima in an uncontrolled way.

A spacer wafer provided a separation of 250 μm between the two trap electrode layers. These three wafers sat atop a 500 μm thick 'filter board', upon which in-vacuum RC filtering components were mounted. The 'bias wafer' resembled the 'top' and 'bottom' wafers but with a single continuous control electrode extending along all sides of the main channels. The bias wafer sat below the filter board and was used to compensate stray electric fields along $\hat{y}$.

Gauge pins were used to help align the wafers during assembly. A misalignment error of approximately $0.22°$ was measured between the $\hat{z}$ axes of the two electrode wafers, and this error was included in the computer model of the trap used to determine the appropriate transport potentials.

The electrode layout of the array is depicted in Fig. 3 and consisted of 46 control electrodes that produced
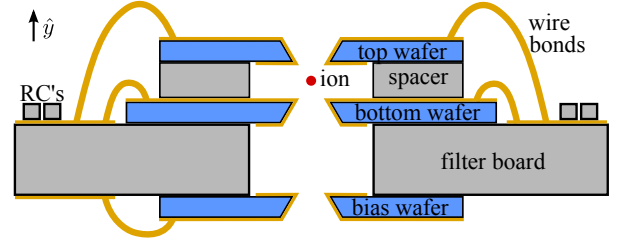

FIG. 1: A cross sectional view (not to scale) of the five-wafer stack, in the $\hat{x}, \hat{y}$ plane at the experiment zone ($\mathcal{E}$). Each wafer had a channel cut through it to define the electrode structure and to provide a path for laser beams to pass through the wafer stack. The top and bottom wafers provided the confining potential; the ions were trapped between these electrodes as indicated. The RC low-pass filters were surface-mounted to the filter board with gold ribbon attached by use of resistive welds. The bias wafer was a single electrode used to null stray electric fields along $\hat{y}$. Gold (represented in yellow) was coated on the top side of the trap wafers and wrapped around to the bottom side, and vice-versa for the bias wafer. Gold wire bonds connected traces on the trap wafers to traces on the filter board.
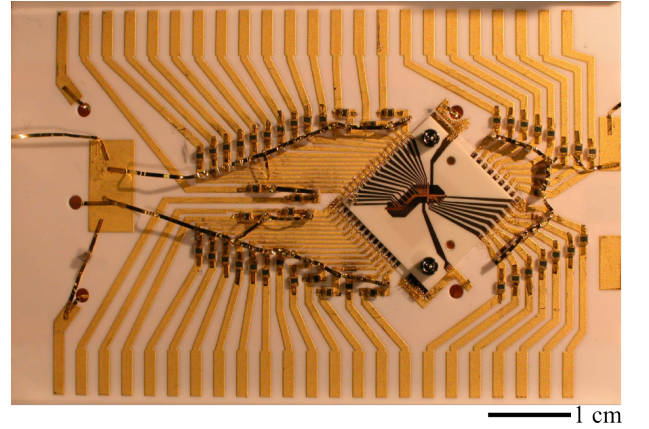

FIG. 2: Top view of the filter board and trap wafers. The filter board fills the entire image, while the top wafer is the rotated square visible on the right of the image. Cap screws, visible in two corners of the top wafer, held the wafer stack together. Wire bonds connected the filter board traces to the top and bottom trap wafers. Surface-mount resistive and capacitive elements on the filter board provided filtering for the control potentials (see Fig. 10).

18 possible trapping zones. The experiment zone, $\mathcal{E}$, was chosen as the zone where the ions interacted with lasers for cooling and qubit operations. In addition to $\mathcal{E}$, zones $\mathcal{F}$, $\mathcal{V}$, and $\mathcal{C}$ (at the center of the junction) composed the four destinations of the transport protocols. The final zone of interest was the load zone, $\mathcal{L}$, where the ions were initially trapped.

The trap dimensions were similar to those in Refs. [13, 21]. The width of the channel between the rf and control electrodes was 200 μm, except near $\mathcal{L}$, where it increased to 300 μm to increase the volume of the loading zone and,
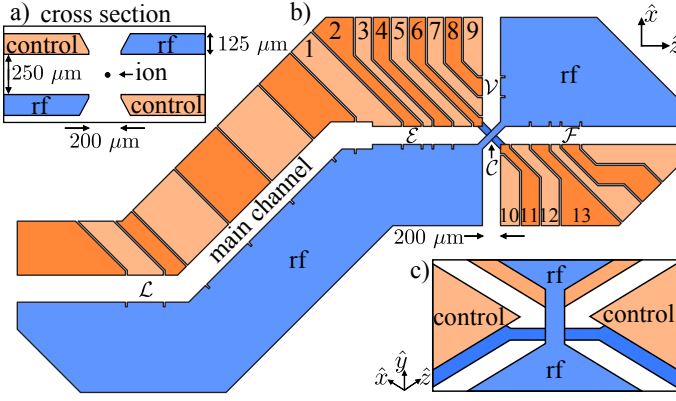
FIG. 3: (a) Cross-sectional view of the two layers of electrodes in the X-junction array. (b) Top view of the electrode layout, with the rf electrodes indicated, and all other (control) electrodes held at rf ground. The bottom trap wafer, which sat below these electrodes, had a nearly identical set of electrodes but with rf and control electrodes exchanged across the main channel. Ions were trapped in the main channels between the rf and control electrodes. Forty-six control electrodes (some of which are numbered for reference) supported 18 different trapping zones. The load zone ($\mathcal{L}$), the main experiment zone ($\mathcal{E}$), the vertical zone ($\mathcal{V}$), the horizontal zone ($\mathcal{F}$) and the center of the junction ($\mathcal{C}$) are labeled. (c) Schematic of the rf bridges from an oblique angle (not to scale).
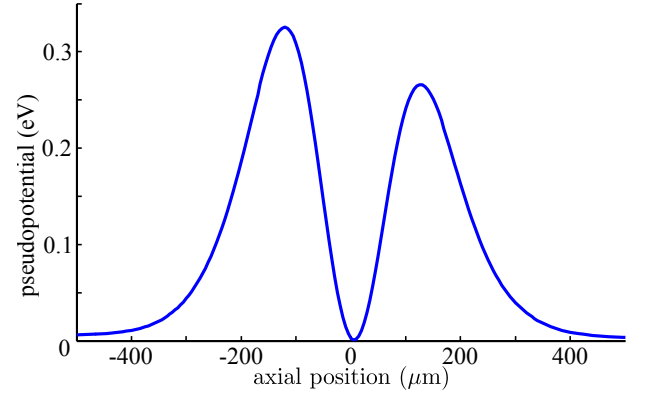

FIG. 4: Simulated pseudopotential barriers along the z axis produced by the rf bridges in the X-junction, with 0 being the junction's center. Here, we assumed $V_{\rm rf} \approx 200$ V and $\Omega_{\rm rf} \approx 2\pi \times 83$ MHz. The asymmetry between the two barriers was due to a slight misalignment of the trap wafers.
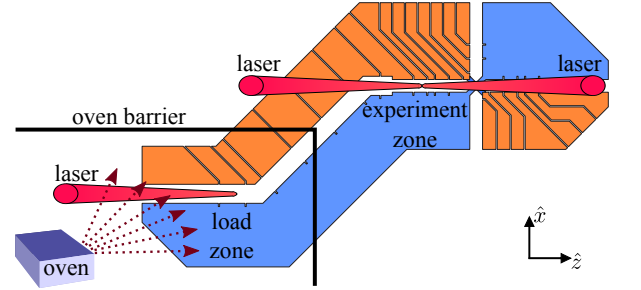

FIG. 5: A Be oven was positioned out of the plane of this figure in the positive y direction (above the trap) and could be heated to produce a flux of neutral Be. This Be would then travel down onto the trap, with a portion of the flux passing into trap's main channel at the load zone. Copropagating photoionization and Doppler-cooling laser beams intersected the Be in the load zone at $45°$ to the xz plane of the page and parallel to $-\hat{y} + \hat{z}$. An 'L'-shaped oven barrier obscured the line-of-sight between the oven flux and the zones used during the transport experiments to prevent neutral Be from accumulating on the surfaces of the electrodes near the junction. This barrier was positioned just above the trap electrodes, extending 1.6 cm along $\hat{y}$ out of the plane of the page. Additional laser access was available for beams passing through $\mathcal{E}$ (at $45°$ to the xz plane) allowing for cooling, detection, and gate operations at $\mathcal{E}$.

with it, the loading probability. Most control electrodes extended 200 μm along the trap axis, but those nearest to the junction were 100 μm wide to ensure sufficient control when ions were transported in this region.

At $\mathcal{C}$, two main channels crossed to form an X-junction, and two rf bridges connected the rf electrodes on opposite sides of that junction (one on the top trap wafer and one on the bottom). Without such bridges, the array would not have provided harmonic three-dimensional confinement at the center of the junction [22, 23]. The widths of the bridges were 70 μm, though the trapping potential was not strongly dependent on this dimension.

These bridges introduced four axial pseudopotential barriers, one in each of the entrances to the junction (along $\pm\hat{x}$ and $\pm\hat{z}$). Figure 4 shows the two simulated pseudopotential barriers along the $\hat{z}$ legs in the X-junction array going toward $\mathcal{E}$ and $\mathcal{F}$ (the asymmetry was due to the trap misalignment mentioned above). The height of these barriers was a significant fraction of the transverse pseudopotential trapping depth and was approximately 0.3 eV for ^{9}Be$^+$, with rf potential of $V_{\rm rf} \approx 200$ V (peak amplitude) and frequency $\Omega_{\rm rf} \approx 2\pi \times 83$ MHz. At the apex of the barriers, just outside the center of the junction, the pseudopotential was anti-confining in the axial direction but still harmonically confining in the two radial directions. It was possible to use the control electrodes to overwhelm this anti-confinement and produce a 3D harmonic confining potential at all points along the axis of the array.

Zone $\mathcal{E}$ was positioned far (880 μm) from the junction

to reduce the residual slope of the pseudopotential barrier in this zone. The amplitude of the axial pseudopotential at $\mathcal{E}$ was estimated, by use of computer models, to be 2.9×10^{-5} eV with a 8.7×10^{-8} eV/μm axial gradient, which would give rise to an axial 'micromotion' amplitude of 47 nm at the drive amplitude specified above.

Ions were loaded into the array from a flux of neutral Be that passed through $\mathcal{L}$ and was photoionized with a mode-locked laser that after two stages of doubling produced 235 nm resonant with the S-to-P transition of neutral Be. To help prevent buildup of neutral Be from the beam in other regions of the array, $\mathcal{L}$ was located suffi-

ciently far from $\mathcal{E}$. In addition $\mathcal{L}$ was displaced along x from $\mathcal{E}$, by use of two $135°$ bends in the main channel, to allow an 'L'-shaped stainless-steel shield to be placed 0.5 mm above the trap wafers, preventing neutral Be from striking the experiment zone while allowing laser access, as shown in Fig. 5. Transporting ions through such $135°$ bends is relatively straightforward, and we were able to easily transport ions between $\mathcal{L}$ and $\mathcal{E}$.

Whenever an ion was lost, a new ion was loaded into $\mathcal{L}$ and immediately transferred to $\mathcal{E}$. It was also possible to use zone $\mathcal{L}$ as a reservoir zone, where extra ions were loaded and held in reserve until needed to replace ions lost in the experiment region. This allowed the loading process to be performed less often, which avoided heating the neutral Be oven and the concomitant degradation of the vacuum. Potentially many ions could be simultaneously stored in such a zone, though we only stored a small number and did not regularly make use of this feature of the trap. By enabling a better vacuum, a reservoir can significantly increase ion lifetime. In this scenario, it is desirable to maintain Doppler cooling in $\mathcal{L}$ to extend the ion lifetime.

III. TRANSPORT POTENTIALS

The first demonstrations of ion transport in a multi-zone trap involved moving an ion along a linear array [12]. A protocol where two ions were placed in a single trapping well and separated into two wells or combined from two wells into a single well was also demonstrated [12, 13]. Since then, transport through linear arrays has been extended to other contexts [14, 16, 17], including transport through a junctions [1, 18–20] and switching of ion order [17, 18].

Here we outline the process used to calculate the time-series of control potentials, or 'waveforms', used to transport ions through the X-junction. This same basic procedure would be generally applicable to many ion-transport situations. The goal was to move ions quickly, over long distances, while maintaining low excitation of the ion's secular motion in its local potential, and traversing non-trivial potential landscapes such as those near junctions. Ideally, the ion should move along the axial direction of the array while remaining at the transverse pseudopotential minimum. The control electrodes were used to create an overall harmonic trapping well whose minimum moved along this desired trajectory. The procedure for determining waveforms can be broken down into four steps: modeling the trap, determining the constraints, solving for the appropriate potentials, and assigning the time dependence of potentials.

An electrostatic model of the trap was constructed by use of boundary element method (BEM) software [24, 25]. For each of N electrodes, the model was run once, applying 1 V to the nth given electrode while grounding all other electrodes. The potential resulting from each of these voltage configurations, $\tilde{\phi}_n(\mathbf{r})$, was extracted (in the form of a 5 μm grid) in the region through which the ion would pass. These individual electrode potentials could then be weighted by the actual voltage applied to the electrode, V_n, and summed to find the total potential:

$$\Phi(\mathbf{r}) = \phi_{\text{ps}}(\mathbf{r}) + \sum_{n=1}^{N} V_n \tilde{\phi}_n(\mathbf{r}). \qquad (1)$$

Here we have included the contribution of the rf pseudopotential ϕ_{ps}. The pseudopotential was found by first modeling the rf potential $\tilde{\phi}_{\text{rf}}$ as if it were a *static* potential at 1 V. Then an additional step was used to convert the rf potential into a time-independent pseudopotential by use of

$$\phi_{\text{ps}}(\mathbf{r}) = \frac{q}{4m\Omega_{\text{rf}}^2} \left(V_{\text{rf}} \nabla \tilde{\phi}_{\text{rf}}(\mathbf{r}) \right)^2, \qquad (2)$$

where V_{rf} was the peak voltage applied to the rf electrode, and q and m are the charge and mass of $^9\text{Be}^+$, respectively. (Throughout this section, all ϕ potentials (including ϕ_{ps}) are reported as electric potentials (in units of V) and not energy potentials (units of eV); these are related by a factor of q.)

The waveform was built up from a string of individual solutions, where each solution satisfied a set of constraints on the trapping potential centered at a certain position. These constraints are defined below, but relate to defining the secular frequencies and orientation of the principle axes of the potential. By advancing that position by 5 μm along the intended ion trajectory for each subsequent solution, the series of potential steps was created that moved the potential well along the sequence of positions. In theory, the constraints can be set to completely define a harmonic potential localized at the desired position, while also constraining the three secular frequencies and the orientation of the principal axes. This would imply nine constraints, which we assume for now, though below we will relax some of these constraints when solving for the experiment waveforms.

To produce a trapping potential, $\Phi(\mathbf{r})$, with a minimum at $\mathbf{r}_0 = (x_0, y_0, z_0)$, we enforce

$$\nabla \Phi(\mathbf{r}_0) \doteq 0, \qquad (3)$$

where $\doteq$ is used to mean 'constrained to be true'.

The Hessian matrix,

$$\mathcal{H}(\mathbf{r}_0) \equiv q \begin{bmatrix} \frac{\partial^2}{\partial x^2} & \frac{\partial^2}{\partial x \partial y} & \frac{\partial^2}{\partial x \partial z} \\ \frac{\partial^2}{\partial y \partial x} & \frac{\partial^2}{\partial y^2} & \frac{\partial^2}{\partial y \partial z} \\ \frac{\partial^2}{\partial z \partial x} & \frac{\partial^2}{\partial z \partial y} & \frac{\partial^2}{\partial z^2} \end{bmatrix} \Phi(\mathbf{r}_0), \qquad (4)$$

can be used to extract the remaining six parameters of the harmonic potential: the eigenvalues λ_i of $\mathcal{H}(\mathbf{r}_0)$ are related to the secular frequencies, $\lambda_i = m\omega_i^2$ and the eigenvectors point along the principal axes. By completely constraining the Hessian, we constrain these quantities. Note that the Hessian is symmetric ($\mathcal{H} = \mathcal{H}^{\text{T}}$), and has only six independent entries.

It is most convenient to evaluate the Hessian in the frame of the desired principal axes, (x', y', z'), in which case the Hessian constraint equation simplifies to

$$\mathcal{H}(\mathbf{r}_0) \doteq m \begin{bmatrix} \omega_{x'}^2 & 0 & 0 \\ 0 & \omega_{y'}^2 & 0 \\ 0 & 0 & \omega_{z'}^2 \end{bmatrix}, \qquad (5)$$

where diagonal entries constrain the desired secular frequencies $(\omega_{x'}, \omega_{y'}, \omega_{z'})$, and the off-diagonal entries constrain the principal axes to point along (x', y', z'). If the Hessian is evaluated in a different basis, the right-hand side of Eq. (5) will not be diagonal, and the frequency and axis constraints are mixed. Nonetheless, an appropriate choice for the right-hand side can still be made in that case [26]. From here on, we assume $(x, y, z) = (x', y', z')$.

In the interest of compact nomenclature, it is convenient to define several column vectors:

$$\mathbf{V} \equiv \begin{bmatrix} 1 & V_1 & V_2 & \dots & V_N \end{bmatrix}^{\mathrm{T}} \qquad (6)$$

and

$$\Psi(\mathbf{r}) \equiv \begin{bmatrix} \phi_{\mathrm{ps}}(\mathbf{r}) & \tilde{\phi}_1(\mathbf{r}) & \tilde{\phi}_2(\mathbf{r}) & \dots & \tilde{\phi}_N(\mathbf{r}) \end{bmatrix}^{\mathrm{T}}, \quad (7)$$

where $\mathbf{A}^{\mathrm{T}}$ denotes the transpose of $\mathbf{A}$ and $\Phi(\mathbf{r}_0) = \Psi^{\mathrm{T}}(\mathbf{r}_0)\mathbf{V}$. Finally, we define the 12-component operator

$$\mathcal{P} \equiv \begin{bmatrix} \frac{\partial}{\partial x} & \frac{\partial}{\partial y} & \frac{\partial}{\partial z} & \frac{\partial^2}{\partial x^2} & \frac{\partial^2}{\partial x \partial y} & \frac{\partial^2}{\partial x \partial z} \\ \\ \frac{\partial^2}{\partial y \partial x} & \frac{\partial^2}{\partial y^2} & \frac{\partial^2}{\partial y \partial z} & \frac{\partial^2}{\partial z \partial x} & \frac{\partial^2}{\partial z \partial y} & \frac{\partial^2}{\partial z^2} \end{bmatrix}^{\mathrm{T}}, \qquad (8)$$

where the first three components are the gradient and the next nine components are the Hessian operator.

The nine position, frequency, and axis constraints defined by Eqs. 3 and 5 can be assembled into one equation:

$$\mathbf{C}_1\big(\mathcal{P} \otimes \Psi^{\mathrm{T}}(\mathbf{r}_0)\big)\mathbf{V} \doteq \mathbf{C}_2, \qquad (9)$$

where $\mathbf{C}_1$ is a $j \times 12$ matrix and $\mathbf{C}_2$ is a $j \times 1$ column vector, where $j = 9$ for this example.

The position constraints in Eq. 3 can be reconstructed by using $\mathbf{C}_1$ to pick out the three gradient components of $\mathcal{P}$ and $\mathbf{C}_2$ to set them to zero. The constraints in Eq. 5 can be treated in a similar manner. Thus, to encode the nine desired constraints, we use

$$\mathbf{C}_1 = \begin{bmatrix} 1 & 0 & 0 & 0 & 0 & 0 & 0 & 0 & 0 & 0 & 0 & 0 \\ 0 & 1 & 0 & 0 & 0 & 0 & 0 & 0 & 0 & 0 & 0 & 0 \\ 0 & 0 & 1 & 0 & 0 & 0 & 0 & 0 & 0 & 0 & 0 & 0 \\ 0 & 0 & 0 & 1 & 0 & 0 & 0 & 0 & 0 & 0 & 0 & 0 \\ 0 & 0 & 0 & 0 & 0 & 0 & 1 & 0 & 0 & 0 & 0 & 0 \\ 0 & 0 & 0 & 0 & 0 & 0 & 0 & 0 & 0 & 0 & 0 & 1 \\ 0 & 0 & 0 & 0 & 1 & 0 & 0 & 0 & 0 & 0 & 0 & 0 \\ 0 & 0 & 0 & 0 & 0 & 1 & 0 & 0 & 0 & 0 & 0 & 0 \\ 0 & 0 & 0 & 0 & 0 & 0 & 0 & 1 & 0 & 0 & 0 & 0 \end{bmatrix} \qquad (10)$$

and

$$\mathbf{C}_2 = \begin{bmatrix} 0 \\ 0 \\ 0 \\ (m/q)\omega_x^2 \\ (m/q)\omega_y^2 \\ (m/q)\omega_z^2 \\ 0 \\ 0 \\ 0 \end{bmatrix}. \qquad (11)$$

Additional white space has been inserted in both equations to aid the reader by separating the position, frequency, and principal axis constraints into groups in the vertical direction, as well as separating the gradient and Hessian components of Eq. 10 in the horizontal direction.

Once $\mathbf{C}_1$ and $\mathbf{C}_2$ are determined, Eq. (9) can be solved for $\mathbf{V}$ by inverting $\mathbf{C}_1\big(\mathcal{P} \otimes \Psi^{\mathrm{T}}(\mathbf{r}_0)\big)$, thus determining the control voltages that create the desired trapping potential. This inversion may not be strictly possible, as is the case when the number of constraints does not equal the number of control potentials, leading to an over- or under-determined problem. Also, we are interested only in solutions where the magnitudes of all control voltages are smaller than a maximal voltage $V_{\max}$ (for our apparatus, $V_{\max} = 10$ V). To achieve this, we use a constrained least-squares optimization algorithm, as described in Ref. [27], to calculate

$$\min_{|V_i| \le V_{\max}} \big| \mathbf{C}_1\big(\mathcal{P} \otimes \Psi^{\mathrm{T}}(\mathbf{r}_0)\big)\mathbf{V} - \mathbf{C}_2 \big|^2. \qquad (12)$$

In cases where Eq. (9) is over-constrained, this method yields a "best-fit" $\mathbf{V}$. When Eq. (9) is under-constrained, as is usually the case for large trap arrays with many electrodes, it returns a null space in addition to $\mathbf{V}$, which can be added to $\mathbf{V}$ to find multiple independent solutions.

Nine constraints were used above, but many are unnecessary. For QIP in a linear trap array, constraining the axial mode frequency and orientation is often sufficient. Parameters for the other two modes are less important and often achieve reasonable values without being constrained, in which case they can be omitted from the constraint matrices.

In addition to explicitly defined user constraints, there are implicit physical and geometric constraints that must be considered. As an example, take the three secular frequencies of the ion, ω_x, ω_y, and ω_z. These frequencies result from a hybrid potential that includes both pseudopotential and control potentials. The contributions from both potentials can be separated mathematically into components, $\omega_{\mathrm{rf},i}$ and $\tilde{\omega}_i$ respectively, which add in quadrature to give the overall frequency: $\omega_i^2 = \tilde{\omega}_i{}^2 + \omega_{\mathrm{rf},i}^2$. (An imaginary frequency component would imply anti-trapping, while a real component yields trapping.) The control electrodes produce a quasi-static electric field, which Laplace's equation requires to be divergenceless.

This places a physical constraint on the frequencies components due to the control potential, namely $\sum_{i=1}^{3} \tilde{\omega}_i^2 = 0$. Thus, Laplace's equation permits only certain combinations of the secular frequencies. For a *linear* Paul trap, where $\omega_{\mathrm{rf},z} = 0$, the secular frequencies must obey

$$\omega_x^2 + \omega_y^2 + \omega_z^2 = 2\omega_{\mathrm{rf}}^2, \tag{13}$$

where ω_{rf} is the pseudopotential radial trapping frequency.

The trap geometry can place constraints on the trapping potentials, as well. For example, in traps where the geometry contains some symmetry, the potentials must preserve that symmetry. Care must be exercised to ensure that user-defined constraints do not contradict physical or geometry constraints, as this will invalidate the solution.

Though we invoke only position, frequency, and orientation constraints here, other varieties of user-defined constraints can be easily included with this framework, and a more complete discussion of these constraints is presented in [26]. The constraints used to construct the waveforms in the X-junction array were as follows:

1. The position of the potential minimum was constrained in three directions to be at $\mathbf{r}_0$.

2. One of the principal axes was constrained to lie along the trap axis (which involves two constraints on axes orientation).

3. The ion axial frequency was constrained (usually to 3.6 MHz).

4. The voltages were constrained to be between ± 10 V (to conform to the limits of the voltage supplies used in the experiment).

This relatively sparse set of constraints tended to give good solutions at most locations considered. Item 4 is an inequality constraint that is easily implemented by use of the constrained least-squares method.

When solving waveforms that transport across multiple zones, $\mathbf{V}$ can become discontinuous from step to step, especially when transitioning between sets of control electrodes. These jumps occur when an under-constrained problem (with null space rank > 0) has multiple linearly-independent solutions and the algorithm returns a different solution from one step to the next: during transport there will be some position at which it is suddenly easier to produce the desired potential using a new combination of electrodes. In principle, such jumps should not have adverse effects on the potential at the ion, as the potentials on both side of the jump fulfill the same constraints and should transition smoothly. However, since the potentials on the electrodes are filtered, we would expect the potential at the ion to experience a transitory jump during the transition.

These solution jumps can be handled by various means. We used the constrained least-squares method to seed each new solution with the solution of the previous step while introducing a cost for deviating from the previous solution by replacing Eq. 12 with

$$\min_{|V_i| \leq V_{\max},\ |V_i - V_{i,\mathrm{last}}| \leq \alpha} \left| \mathbf{C}_1 \big(\mathcal{P} \otimes \Psi^{\mathrm{T}}(\mathbf{r}_0) \big) \mathbf{V} - \mathbf{C}_2 \right|^2,$$
$$(14)$$

for a positive constant α. This removes the need for iteratively choosing weights to keep the voltages within bounds, as suggested in Ref. [25]. This forced the jump transition to be extended over multiple steps, rather than allowing a discontinuous jump. Another approach is to average the two $\mathbf{V}$'s on each side of the discontinuity, taking advantage of the linearity of the equations, to produce an intermediate solution that still satisfies the constraints [28]. Performing several steps of such averaging will smooth the jump. Alternately, trial and error can often be used to determine a set of constraints that does not produce a jump, but this can require significant effort.

1. Transport timing

If the spatial interval between steps in the waveform is small enough, the potential, once applied to the electrodes, will move smoothly from step to step [26]. The velocity of the potential well (and, thus, the ion) is controlled by the rate at which the waveform steps are updated on the electrodes. In our case, the control potentials were supplied by digital-to-analog converters (DACs) that had a constant update rate $R_{\mathrm{DAC}} = 480$ kHz and the number of update steps was adjusted to change the velocity.

Different velocity profiles have been considered for minimizing excitation while transporting [29, 30]. In this report, the ions were usually transported by use of a constant velocity with equally spaced waveform steps. This could potentially lead to the ion being 'kicked' as the velocity jumps at the beginning and end of the transport, resulting in motional excitation. However, these velocity jumps were smoothed by low-pass filters placed on the control potentials (see Sec. V B). A smoother 'sinusoidal' velocity profile was also tested but was abandoned after observing no discernible difference in the amount of motional excitation by use of the different profiles. This suggests that both transport protocols were well within the adiabatic regime at the speeds used.

Low-pass filtering (160 kHz corner in our case) can also potentially distort the waveforms when transporting quickly, placing an upper limit on the ion speed. However, the practical speed limit was set by the combination of the maximum update rate of the digital-to-analog converters and the number of update points required to accurately produce a continuous harmonic potential in the region of the pseudopotential barrier. This limit was experimentally determined for each waveform by adjusting
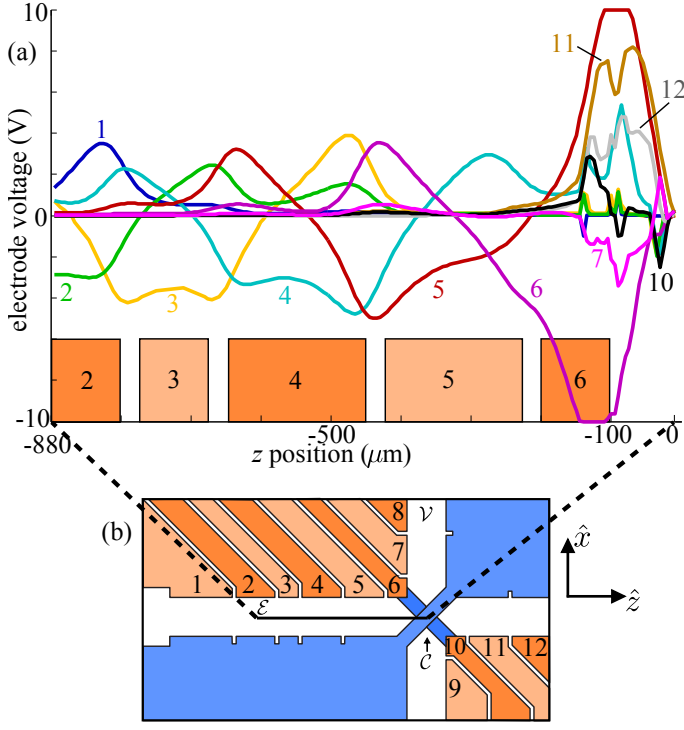
FIG. 6: (a) The waveform (as a function of position rather than time) used when transporting an ion from the experiment zone, located at $z = -880$ μm, to the center of the junction at $z = 0$ μm. We plot voltage versus the z position of the minimum of the trapping potential during the transport. The locations of the electrodes near the junction are depicted, along with their electrode number, by the rectangles in the bottom of the figure. The region from -100 to 0 μm is inside of the junction. The voltage traces are numbered to show which electrode they correspond to. Electrodes 8 and 9 remain near 0 V and are omitted for clarity. In addition, the potentials applied to the control electrodes on the bottom wafer are not displayed, as they are nearly identical to those applied on the top wafer. (b) A schematic of the trap, showing the range over which this waveform transported.

the number of update points until minimum motional excitation was achieved. If faster DACs are available and distortion of the waveforms due to low-pass filtering is of concern, the waveform can be pre-compensated to account for these distortions and produce the desired waveform at the ion.

The waveforms used to transport from $\mathcal{E}$ to $\mathcal{C}$ are displayed in Fig. 6 as a function of the position of the minimum of the trapping potential (the ion's location). The potentials applied to the lower trap-wafer control electrodes (on opposite sides of the main channel) were nearly identical and are omitted for clarity. These waveforms could be run left to right to transport an ion 880 μm from $\mathcal{E}$ to $\mathcal{C}$, or they could be run in reverse. The waveforms that transported ions into the other two branches of the junction (to $\mathcal{F}$ and $\mathcal{V}$) were similar to this waveform due to the approximate symmetry of the trap.

In a typical transport, the potential minimum was

moved at a constant velocity, and there was a direct linear relationship between the location of the minimum (horizontal axis of Fig. 6(a)) and the time elapsed since the beginning of the transport. The typical transport duration for the waveforms in Fig. 6(a) was approximately 165 μs, with 50 μs to cross the pseudopotential barrier.

Some control potentials reached the ± 10 V limit placed by use of the constrained least-squares method while traversing the pseudopotential barrier near the junction. Other control potentials had sharp and abrupt changes, which resulted from the constraint in Eq. 14 that prevented 'solution jumping' by defining how much a given waveform step can deviate from the previous step. Instead of jumping, the voltages ramped linearly over several steps. Although these individual potentials were not smooth in time, they were continuous, which was sufficient to ensure that the overall potential experienced by the ion evolved smoothly.

The axial frequency was chosen to be 3.6 MHz and was held constant during much of the transport starting at $\mathcal{E}$ and moving toward $\mathcal{C}$ (Fig. 7). The frequency was (adiabatically) linearly ramped to 4.2 MHz as the ion approached the apex of the pseudopotential barrier, making the ion less susceptible to rf-noise heating of the secular motion (see Sec. V A). The value 4.2 MHz was the maximum axial frequency attainable at the apex due to the strong anti-confinement of the pseudopotential at that location and the ± 10 V limit of the DACs providing the control potentials. The axial frequency then continued to increase as the ion descended the barrier, reaching a final value of 5.7 MHz at $\mathcal{C}$. At this location, all control potentials were 0 V and the pseudopotential provided all the trapping, resulting in near-degenerate 5.7 MHz confinement along the $\hat{x}$ and $\hat{z}$ directions, while the $\hat{y}$ secular frequency was 11.3 MHz. When transporting multiple ions in the same potential well, it would be preferable to break the frequency degeneracy at $\mathcal{C}$ to ensure well-defined axes for the ions. In practice, the motional excitation rates when moving pairs of ions were still relatively low despite the near degeneracy at $\mathcal{C}$ (see Table II).

IV. TRANSPORT EXPERIMENTS

The transport experiments were performed with ^{9}Be$^+$ ions inside a vacuum system with a pressure of $p < 5 \times 10^{-11}$ Torr $= 7 \times 10^{-9}$ Pa. A 1.3×10^{-3} T magnetic field was applied to split the Zeeman states, and the ions were optically pumped to the $^2S_{1/2} |F = 2, m_F = -2\rangle$ state (henceforth $|2, -2\rangle$). Manipulation of the ^{9}Be$^+$ ion motional and internal states used the techniques of Refs. [6, 31]. Two-photon stimulated-Raman transitions enabled coherent transitions between the qubit states $|2, -2\rangle$ and $|1, -1\rangle$ at frequency $\omega_0 \approx 2\pi \times 1.28$ GHz. In addition, by tuning the difference frequency of the Raman beams to $\omega_0 \pm \omega_z$, it was possible to drive a blue(red)-sideband transition: $|2, -2\rangle |n\rangle \leftrightarrow |1, -1\rangle |n \pm 1\rangle$. Here $|n\rangle$ is a Fock state of a
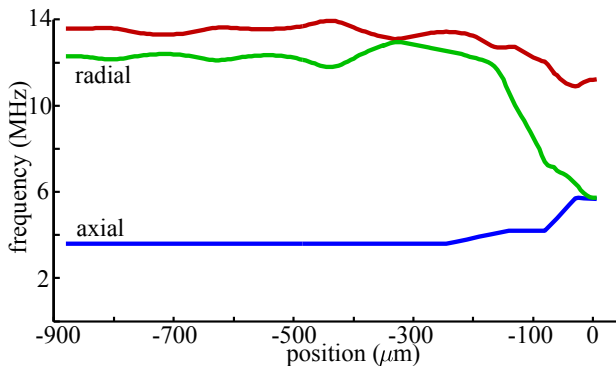
FIG. 7: Predicted secular frequencies as a function of position corresponding to the waveform in Fig. 6. The axial frequency along $\hat{z}$ was constrained to be 3.6 MHz during the majority of the transport, while the radial frequencies were unconstrained. As the ion ascended the pseudopotential barrier, the axial frequency linearly ramped up to 4.2 MHz. Beyond the apex of the barrier, a second linear ramp was applied to bring the frequency up to 5.7 MHz. As the ion approached the center of the junction, the x and z frequencies became nearly degenerate.

selected motional mode. Ground-state cooling was performed by use of a series of red-sideband pulses, followed by repeated optical pumping to $|2, -2\rangle$. State detection was performed using state-dependent resonance fluorescence, where predominantly the $|2, -2\rangle$ state fluoresces.

Each transport began by cooling an ion (or ion pair) in $\mathcal{E}$ to the motional ground state. The ion was then transported into or through the junction and returned to $\mathcal{E}$. Three transports patterns were used: $\mathcal{E}$-$\mathcal{C}$-$\mathcal{E}$ moved to $\mathcal{C}$ and back, while $\mathcal{E}$-$\mathcal{C}$-$\mathcal{F}$-$\mathcal{C}$-$\mathcal{E}$ and $\mathcal{E}$-$\mathcal{C}$-$\mathcal{V}$-$\mathcal{C}$-$\mathcal{E}$ moved to $\mathcal{F}$ and $\mathcal{V}$, respectively, before returning to $\mathcal{E}$. The $\mathcal{E}$-$\mathcal{C}$-$\mathcal{E}$ transport moved the ion 1.76 mm, while $\mathcal{E}$-$\mathcal{C}$-$\mathcal{F}$-$\mathcal{C}$-$\mathcal{E}$ and $\mathcal{E}$-$\mathcal{C}$-$\mathcal{V}$-$\mathcal{C}$-$\mathcal{E}$ moved the ion 3.52 mm and 2.84 mm, respectively. Once the ion returned to $\mathcal{E}$, the motional excitation was determined by measuring the asymmetry in red- and blue-sideband Raman transitions [31, 32].

To determine the single-ion transport success rate for $\mathcal{E}$-$\mathcal{C}$-$\mathcal{F}$-$\mathcal{C}$-$\mathcal{E}$ transports, two sets of 10,000 consecutive transport experiments were performed [1], but with the imaging system focused on $\mathcal{E}$ in the first set and on $\mathcal{F}$ in the second. The first set verified that the ion successfully returned to $\mathcal{E}$ every time. The second set verified that the ion always reached $\mathcal{F}$ at the intended time. Together, these sets of experiments imply the success rate for going to $\mathcal{F}$ and returning to $\mathcal{E}$ exceeded 0.9999. The procedure was repeated for $\mathcal{E}$-$\mathcal{C}$-$\mathcal{V}$-$\mathcal{C}$-$\mathcal{E}$, with the same result. The $\mathcal{E}$-$\mathcal{C}$-$\mathcal{E}$ transport can not be verified in the same manner because the bridges obscure the ion at $\mathcal{C}$, but since the ion must transport through this location to reach $\mathcal{F}$ and $\mathcal{V}$, the reliability should be no worse.

Ion lifetime, and thus transport success probability, was ultimately limited by ion loss resulting from background-gas collisions [6]. With this in mind, the ion loss rate during transport was not larger than that for

a stationary ion (~ 0.5/hr). Having observed millions of successive round trips for all three types of transport, combining all losses implies a transport success probability of greater than 0.999995[45]. Since transport comprised a small fraction of the total experiment duration, many of these losses likely occurred when the ion was not being transported. In one instance, more than 1,500,000 consecutive $\mathcal{E}$-$\mathcal{C}$-$\mathcal{E}$ transports were performed with a single ion.

Loss rates for transported ion pairs were again comparable to stationary pairs (~ 2 per hour). Absolute pair loss rates were higher than those for single ions, presumably due to multi-ion effects [6, 33].

V. EXCITATION OF THE SECULAR MOTION

Excitation of the ion's motion during transport was attributed to two main mechanisms: one due to rf noise near $\Omega_{\rm rf}$ and the other due to excitation from the digital-to-analog converters (DACs).

A. rf-noise heating

Consider a trapping rf electric field with an additional sideband term,

$$\mathbf{E}_{\rm rf}(\mathbf{r}, t) = \mathbf{E}_0(\mathbf{r}) \left[\cos \Omega_{\rm rf} t + \xi_{\rm N} \cos\left(\Omega_{\rm rf} \pm \omega_z\right)t\right], \quad (15)$$

where $\xi_{\rm N} \ll 1$, and $\Omega_{\rm rf} \pm \omega_z$ is at one of the two axial motional sidebands of the ion. In [1], it was shown that the two terms will beat at ω_z to produce a force that can excite the ion's motion. If the second term is not coherent, but instead is broad-spectrum noise, this will lead to excitation of the axial motion at a rate of

$$\dot{\bar{n}}_z = \frac{q^4}{16 m^3 \Omega_{\rm rf}^4 \hbar \omega_z} \left[\frac{\partial}{\partial z} E_0^2(z)\right]^2 \times \left(\frac{S_{V_{\rm N}}(\Omega_{\rm rf} + \omega_z)}{V_{\rm rf}^2} + \frac{S_{V_{\rm N}}(\Omega_{\rm rf} - \omega_z)}{V_{\rm rf}^2}\right), \quad (16)$$

where $S_{V_{\rm N}}(\Omega_{\rm rf} \pm \omega_z)$ is the voltage-noise spectral density at either the upper or lower rf sideband, and $V_{\rm rf}$ is the amplitude of the trapping rf potential being applied to the rf electrodes. $E_0(z)$ is the axial rf electric field amplitude at the location of the ion. This heating mechanism is proportional to the *slope* of the pseudopotential and is significant only in places with a large slope, such as the pseudopotential barriers near the junction (but not in, for example, $\mathcal{E}$).

This heating mechanism was verified in Ref. [1] by measuring the heating rate at various locations along the pseudopotential barrier between $\mathcal{E}$ and $\mathcal{C}$, while spectrally-dense white noise (centered on the lower sideband, $\Omega_{\rm rf} - \omega_z$) was injected onto the trap rf drive. Figure 8 plots the ratio of measured heating rate to estimated injected $S_{V_{\rm N}}$ and theoretical values of this ratio
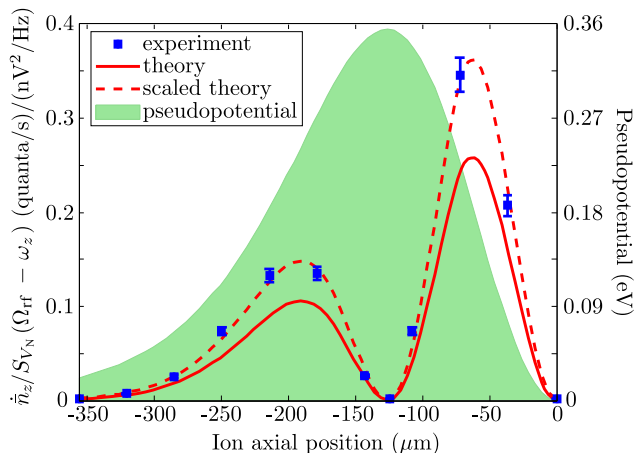
FIG. 8: The ratio of heating rate $\dot{\bar{n}}_z$ to voltage noise spectral density $S_{V_N}(\Omega_{rf} - \omega_z)$ for various locations along the trap axis ($\mathcal{C}$ is located at 0 μm). This figure is reproduced from Ref. [1]. The theoretical prediction used a pseudopotential modeled from electrode geometry and is shown both with and without a scaling parameter ($= 1.4$). The simulated pseudopotential is overlaid in the background, in units of eV. Since heating was gradient dependent, we saw very little heating at the peak of the pseudopotential barrier, even though this was the point of maximum (axial) rf electric field and therefore maximum axial rf micromotion. Nearly identical pseudopotential barriers were present on the other three legs of the junction.

according to Eq. (16) based on simulations of trap potentials, for the ion held at several positions between $\mathcal{E}$ and $\mathcal{C}$. A plot with the theoretical values multiplied by a scaling factor ($= 1.4$) is also included. The deviation of the scaling factor from 1 is not unreasonable due to the difficulty of accurately measuring a variety of experimental parameters.

The motional excitation for full junction transports to $\mathcal{C}$ was observed to decrease as the ion speed was increased, which minimized the exposure to the rf noise while on a pseudopotential slope. This continued up to a maximum speed limit, due to the slow DACs, above which the other excitation mechanism (below) began to dominate. At the optimum speed, the ion spent only approximately 50 μs on each barrier (above 10% of the barrier height).

Another approach to mitigate rf noise is to suppress the sideband noise with better filtering of the applied rf trapping potential. In Ref. [1], the large rf potential ($V_{rf} \approx 200$ V$_{peak}$ at $\Omega_{rf} \approx 2\pi \times 83$ MHz) was provided by a series of tank resonators, which suppressed noise at the motional sidebands (± 3.6 MHz). The primary resonator was a quarter-wave step-up resonator [34] with a loaded $Q = 42$ and corresponding bandwidth (FWHM) of 2 MHz. This resonator extended into the vacuum, with the trap attached to the voltage anti-node. A second half-wave resonator with $Q = 145$ was attached, in series, to the input of the primary resonator, with a 3 dB attenuator in between to decouple the two resonators. The resonant frequencies of the two resonators were tuned to

be equal. This network resulted in an estimated ambient $S_{V_N}(\Omega_{rf} \pm \omega_z)$ of -177 dBc at the ion. In the work reported here, the second resonator was replaced with a pair of half-wave tank resonating cavities. This filter pair provided more than 38 dB suppression at frequencies $\Omega_{rf} \pm 2\pi \times 3.6$ MHz (when not coupled to the primary resonator), an additional suppression of approximately 10 dB over the half-wave filter used in Ref. [1]. S_{V_N} at the ion was not re-measured with this new filter pair, but observed reductions in excitation during transport were consistent with a 10 dB drop in rf noise.

B. DAC update noise

Another primary source of motional excitation was attributed to the 16-bit, ± 10 V DACs that supplied the waveform potentials to the electrodes. The DAC voltages were updated at a constant rate R_{DAC} (≤ 500 kHz), resulting in Fourier components that could excite the ion's motion if $2\pi \times R_{DAC} = \omega_z/J$, for any integer J.

This effect was observed by first preparing the ion in the motional ground state at $\mathcal{E}$ and then transporting toward $\mathcal{C}$. Instead of proceeding all the way to $\mathcal{C}$, the transport was stopped (at $z = -300$ μm) before the axial frequency began to ramp up. Thus, the local potential-well frequency remained approximately constant at $\omega_z = 2\pi \times 3.6$ MHz. The ion was then returned to $\mathcal{E}$. A red-sideband Raman π-pulse for $n = 0$ to $n = 1$ excitation was applied to determine if the ion remained in the ground state [31, 32]. If the ion was excited out of the ground state during transport, the Raman pulse had a certain probability to transfer the ion into the $|1, -1\rangle$ state, which did not fluoresce during detection. If the ion remained in the ground state, this side-band pulse had no effect and the ion remained in the bright $|2, -2\rangle$ state. Thus, fluorescence detection after the side-band pulse could distinguish an excited ion from a non-excited ion.

This experiment was performed for various values of R_{DAC}, and the results are shown in Fig. 9. It was difficult to extract the ion's exact motional state after the transport, but the correlations between the ion's motional excitation and ω_z corresponding to a harmonic of R_{DAC} were evident. The energy gain exhibited a resonance at several values for $R_{DAC} = \omega_z/(2\pi J)$ with $J = 8$ to 14. When the number of update steps was increased, while the update rate was held constant (which resulted in an increased transport duration), the bandwidth of these resonances decreased, as expected from a coherent excitation.

Use of an update rate that was incommensurate with the motional frequency ($R_{DAC} \neq \omega_z/(2\pi J)$) minimized this energy gain. However, increasing the transport speed (using the same update rate) required a reduction in the number of waveform steps, which caused the resonances to broaden. Minimizing the rf-noise heating required fast transport, so at the speed that gave the low-
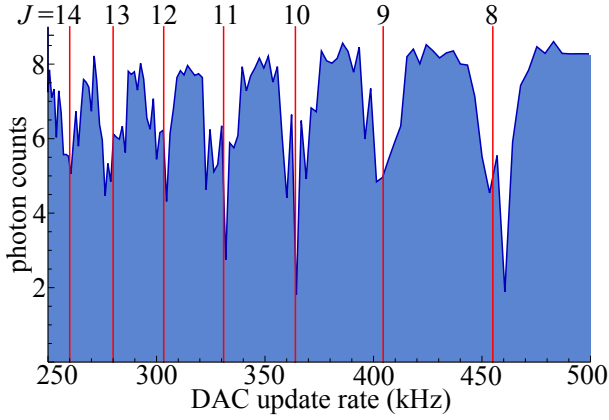
FIG. 9: Plot showing the the number of fluorescence photons detected in a duration of 200 μs following round-trip transport and a subsequent red sideband pulse, for various DAC update rates R_{DAC}. Before transport, the ion was prepared in the motional ground state and then transported through a specific waveform, where $\omega_z = 2\pi \times 3.6$ MHz was maintained during the entire transport. If the ion remained in the ground state after transport, the ion fluorescence was at its maximum value (approximately 8 photon counts detected), but when the ion became motionally excited, the fluorescence dropped. As can be seen, the motion was excited at specific update frequencies that correspond to $R_{\mathrm{DAC}} = \omega_z/(2\pi J)$ for $J = 8$ to 14 (marked by the vertical red lines).

est rf-noise excitation rates, the DAC heating resonances were so broad that they overlapped, and there was no achievable R_{DAC} that would not result in energy gain. The DAC heating effect was further compounded by the fact that the axial frequency was not constant during a full junction transport, making it impossible to achieve $R_{\mathrm{DAC}} \neq \omega_z/(2\pi J)$ for any constant R_{DAC}. The update frequency $R_{\mathrm{DAC}} = 480$ kHz appeared to be most favorable and was used for the results here and in Ref. [1].

Faster DACs capable of $R_{\mathrm{DAC}} > \omega_z/2\pi$ should significantly suppress this motional excitation. Alternatively, aggressive filtering of the DAC output can combat this problem. The results in Ref. [1] used the RC filter network shown in Fig. 10(a), which provided suppression by two orders-of-magnitude over the range of $\omega_z/2\pi$ values used during transport (3.6 to 5.7 MHz), but was not sufficient to completely suppress the DAC heating. Increasing the RC time constant would increase the filtering but would also slow down the rate at which the ion can be transported. Instead, these simple RC filters were replaced with the approximately third-order Butterworth filter [35] shown in Fig. 10(b). (The output impedance of the DAC was < 0.1 Ω and contributed minimally to the filter response.)

A Butterworth filter has a frequency response given by

$$G(\omega) = \frac{1}{|B_n(i\omega/\omega_0)|} = \frac{1}{\sqrt{1 + (\omega/\omega_0)^{2n}}}, \qquad (17)$$

where $B_n(s)$ is the nth-order Butterworth polynomial and ω_0 is the corner frequency. If $n = 1$, the frequency re-
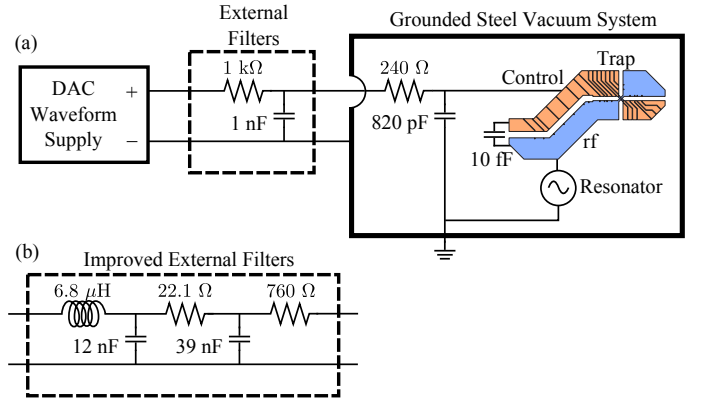

FIG. 10: The control voltages were provided by 40 independent DACs (only one shown here). The DAC output was filtered prior to being applied to the trap electrodes, through a two stage filter seen in (a). The control potentials were referenced to the grounded vacuum system, which served as the rf ground as well. (b) After DAC-update noise was observed to excite the secular motion of the ions, the external filters were replaced by the approximate 3$^{\mathrm{rd}}$-order 'Butterworth' filter shown here.

sponse reduces to a RC frequency response. In the experiments here, such higher-order filters provide stronger noise suppression at ω_z while still allowing fast transport. A comparison of the theoretical response functions for the RC filters used in Ref. [1] and the Butterworth filters used here is shown in Fig. 11. The internal vacuum RC components already on the filter board were taken into account when planning the Butterworth filter, but the external filter components were designed to dominate the filter's response in the frequency range of concern. Thus, the filter was approximately third-order, despite the presence of four components (including the filter board capacitor) with frequency-dependent impedances. The new filters increased the noise filtering by 22 dB at 3.6 MHz and 26 dB at 5.7 MHz. Furthermore, the electric-field noise at the ion due to Johnson noise in the resistive elements of the new filters was less than that for the previous filters for all frequencies of interest. For the transport durations used, these filters did not appreciably distort the waveform.

C. Anomalous noise heating

The 'anomalous heating', which is thought to arise from noisy electric potentials on the surface of the trap [32], was measured to be 40 quanta/s for $\omega_z/2\pi = 3.6$ MHz at $\mathcal{E}$ and was not a significant source of excitation during the transport experiments. For example, we estimate that it should have contributed only 0.007 quanta for $\mathcal{E}$-$\mathcal{C}$-$\mathcal{E}$ transport. To compare the measurements of various ion traps, it has been common to express the heating in terms of the electric field noise
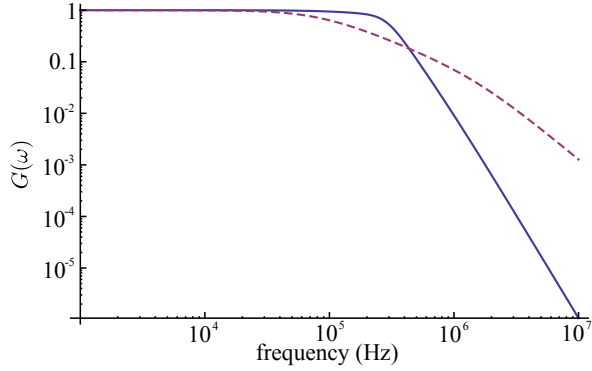
FIG. 11: Theoretical transfer function $G(\omega)$ versus frequency for the original RC filter (dashed) and the improved approximately-'Butterworth' filter (solid), where the new filter had a faster roll-off at high frequency. Since the pass-band extended farther for the new filter, the transport speed could be increased while providing more filtering at the secular frequency (3.6 MHz to 5.7 MHz). Both traces include the RC components inside the vacuum.

with the expression [32]:

$$\dot{\bar{n}}_z = \frac{q^2}{4m\hbar\omega_z} S_E(\omega_z),\qquad(18)$$

where $S_E(\omega_z)$ is the spectral density of electric field fluctuations at the secular frequency. From the results here we found $S_E(2\pi \times 3.6\ \mathrm{MHz}) = 2.2 \times 10^{-13}\ (\mathrm{V/m})^2\mathrm{Hz}^{-1}$, where the distance of the ion to the nearest electrode surface was 160 μm. This result, when compared to other traps as in Refs. [19, 36–38], was significantly below that of most other room-temperature ion traps. The cause of this relatively low heating rate is not known, but surface preparation could be a contributing factor.

D.   Other heating mechanisms

In the experiments here, the transport was slow and the trapping potential changed slowly compared to the motional frequencies, so we did not expect non-adiabatic excitation of the motion. This was supported by observations that the excitation did not decrease as the transport was slowed. For very slow transport, the heating actually increased because the ion spent more time crossing the rf barriers, resulting in increased rf-noise heating. Furthermore, no reduction in heating was observed when a gradual (sinusoidal) velocity profile was used instead of a constant velocity over the entire transport.

The waveforms were produced assuming a specific value of V_{rf} and corresponding pseudopotential. In theory, if the actual V_{rf} does not match the assumed V_{rf}, the axial trapping potential will not be as intended at the barriers. In practice, there was an optimal value for the rf power which resulted in the lowest excitation rates and likely corresponded to the assumed V_{rf}. The rf power was prone to slow drifts over many minutes (likely due

	This work		Ref. [1]	
Transport	Duration (μs)	Energy gain (quanta/trip)	Duration (μs)	Energy gain (quanta/trip)
$\mathcal{E}$-$\mathcal{C}$-$\mathcal{E}$	350	0.053 ± 0.003	310	3.2 ± 1.8
$\mathcal{E}$-$\mathcal{C}$-$\mathcal{F}$-$\mathcal{C}$-$\mathcal{E}$	910	0.18 ± 0.02	630	7.9 ± 1.5
$\mathcal{E}$-$\mathcal{C}$-$\mathcal{V}$-$\mathcal{C}$-$\mathcal{E}$	950	0.18 ± 0.02	870	14.5 ± 2.0

TABLE I: The axial-motion excitation $\Delta\bar{n}$ for a single $^9\mathrm{Be}^+$ ion for three different transports through the X-junction. The results of this work, as well as that of Ref. [1], are given for comparison[a]. The transport duration includes 20 μs for the ion to remain stationary at the intermediate destination (30 μs for the data from Ref. [1]), before returning to $\mathcal{E}$. The energy gain per trip is stated in units of quanta in a 3.6 MHz trapping well where $\Delta\bar{n} = 0.1$ quantum corresponds to 1.6 neV.

[a]The transport durations given in Ref. [1] were reported in error. The correct values are 140 μs for transporting from $\mathcal{E}$ to $\mathcal{C}$, 300 μs to go from $\mathcal{E}$ to $\mathcal{V}$, and 420 μs to go from $\mathcal{E}$ to $\mathcal{F}$. This error did not affect any other results in Ref. [1].

to temperature drifts in the resonators) which resulted in modest increases in motional excitation; it was necessary to occasionally adjust the rf power (every 10 to 30 minutes) and hold it to within < 1 % to achieve the lowest motional-excitation rates. In practice, this was performed by ensuring that the radial secular frequencies at $\mathcal{E}$ remained constant.

E.   Motional excitation rates

The motional excitation for single-ion transports was measured by use of sideband asymmetry measurements [31] after a single pass through the junction, and the results are summarized in Table **??**. These results were significantly better than those in Ref. [1], which are listed for comparison. In Ref. [1], rf noise was estimated to contribute 0.1 to 0.5 quanta of excitation per pass over a pseudopotential barrier, which explained between 3 and 30% of the excitation seen. The remainder of the excitation was attributed primarily to DAC update noise. The new trap rf filters and control electrode Butterworth filters produced the observed reduction in excitation rates.

The transport durations, which were optimized for minimal excitation, are also given in Table **??**. The tabulated durations correspond to the full transport duration including returning to $\mathcal{E}$ (rather than the half-transport reported in Ref. [1]. The durations also include a 20 μs wait at the half-way point ($\mathcal{C}$, $\mathcal{F}$, or $\mathcal{V}$, depending on the transport) for the new results and a 30 μs wait for those from Ref. [1].

Moving pairs of ions in the same trapping well would be useful for both sympathetic cooling and efficient ion manipulation [7]. This type of transport was demonstrated by use of pairs of $^9\mathrm{Be}^+$ ions and the measured motional excitation is reported in Table II. Excitation in both the center-of-mass (COM) and stretch modes was measured. Additional heating mechanisms for multiple

Transport	Energy gain (quanta/trip)		
	This work COM	This work Stretch	Ref. [1] COM
$\mathcal{E}$-$\mathcal{C}$-$\mathcal{E}$	0.39 ± 0.03	0.13 ± 0.02	5.4 ± 1.2
$\mathcal{E}$-$\mathcal{C}$-$\mathcal{F}$-$\mathcal{C}$-$\mathcal{E}$	0.67 ± 0.05	0.53 ± 0.05	16.6 ± 1.8
$\mathcal{E}$-$\mathcal{C}$-$\mathcal{V}$-$\mathcal{C}$-$\mathcal{E}$	0.72 ± 0.06	0.14 ± 0.02	53.0 ± 1.2

TABLE II: The axial-motion excitation $\Delta\bar{n}$ for a pair of $^9\text{Be}^+$ ions transported in the same trapping well. Values for both axial modes of motion (COM and stretch) are reported. The energy gain per trip is stated in units of quanta where the COM frequency is 3.6 MHz and the stretch frequency is 6.2 MHz. Results from Ref. [1] are also given, though only the COM mode excitation was investigated.

ions [6, 33] may explain the higher energy gain observed for the pair. For $\mathcal{E}$-$\mathcal{C}$-$\mathcal{V}$-$\mathcal{C}$-$\mathcal{E}$ transport, the two-ion crystal must rotate from the $\hat{z}$ axis to the $\hat{x}$ axis and back. For the waveforms used, the potential was nearly the same in the $\hat{x}$ and $\hat{z}$ directions at $\mathcal{C}$. Therefore the axes were not well defined throughout the transport, which can lead to an uncontrolled rotation of axes. It is possible that the discrepancy in the excitation between $\mathcal{E}$-$\mathcal{C}$-$\mathcal{F}$-$\mathcal{C}$-$\mathcal{E}$ and $\mathcal{E}$-$\mathcal{C}$-$\mathcal{V}$-$\mathcal{C}$-$\mathcal{E}$ for two ions may have resulted from this uncontrolled rotation at $\mathcal{C}$.

We expect (and observed) less excitation of the stretch mode relative to the COM mode, for two reasons. First, the stretch mode frequency was higher than that of the COM mode ($\omega_{\text{STR}} = \sqrt{3}\omega_{\text{COM}}$). Thus, the filters on the rf and control potentials were more effective at suppressing noise that could excite the stretch mode. Second, a stretch mode can be excited only by a differential force on the two ions, while the COM mode is excited by a force common to both ions. Given the proximity of the ions to each other (a few micrometers) compared to the distance of the ions to the trap electrodes, the relative amplitude of differential forces acting on the ions are expected to be less than common forces.

VI. MITIGATION OF MAGNETIC FIELD FLUCTUATIONS

So far, we have discussed the suppression of undesired excitation of motional degrees of freedom. We now discuss how magnetic-field fluctuations affecting internal-state (qubit) coherence are suppressed in the X-junction trap array.

Decoherence of superpositions of the $|2, -2\rangle$ and $|1, -1\rangle$ qubit basis states occurs both during transport and while the qubit is stationary. Previous experiments demonstrated that junction transport contributed negligibly to decoherence [1]. Magnetic field fluctuations form the dominant contribution to qubit dephasing, yielding typical values (in this trap and others) of less than 100 μs [39]. Use of a magnetic-field-insensitive qubit configuration enables extension of the coherence time to ap-
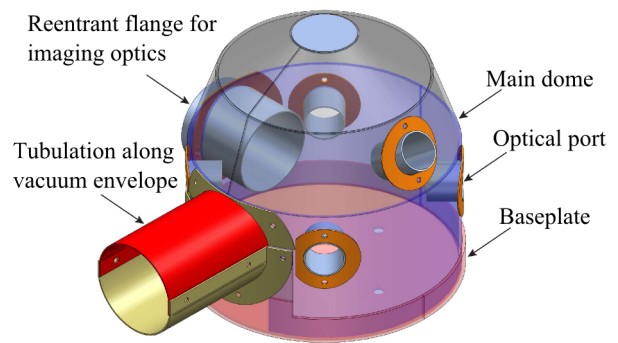

FIG. 12: Mu-metal magnetic shield. The main dome enclosed both the trap and the magnetic-field coils. Cylindrical tubulation extended along a glass vacuum envelope, which corresponds to the $\hat{z}$ direction at the trap. Reentrant flanges minimized field leakage around the imaging and optical access points.

proximately 10 s and can be used with some gate operations such as the Mølmer-Sørenson gate [40], but excludes implementation of $\sigma_z\sigma_z$ gates [39, 41, 42].

To suppress the effects of magnetic field fluctuations, we enclosed the trap and field coils inside a high-magnetic-susceptibility mu-metal shield and implemented an active magnetic field stabilization system. The shield (Fig. 12) was designed for compatibility with the existing trap vacuum envelope and optical systems, and for ease of installation without the need to lift the trap apparatus from the supporting table. A cylindrical body and approximately hemispherical dome were selected based on general guidelines for magnetic shielding and manufacturing constraints. The main body and baseplate of the shield were constructed of 3.2 mm thick, single-layer mu-metal in order to provide maximum shielding of low-frequency magnetic field fluctuations and to suppress magnetic saturation of the mu-metal. This latter constraint arose because part of the field coils defining the quantization axis of the qubits were located approximately 1 cm from the walls, where a calculated field of 4×10^{-3} T was expected for typical operating conditions.

Openings in the shield for optical components or laser beams were outfitted with a reentrant flange fastened to the main body of the shield. The flanges extended both outwards and inwards in the shield in order to maximize flux-line redirection. A target length-to-diameter ratio of 5:1 guided design but was typically not achieved due to geometric constraints arising from the exterior dimensions of the vacuum envelope and the desire to position optical elements as close as possible to the shield for maximum beamline stability. These flanges were designed to be modular, allowing for redesign and replacement if increased shielding became necessary. Magnetic continuity was achieved for all mating flanges by use of internally threaded fasteners, producing a snug contact fit.

The structure was designed to provide a minimum 22 dB shielding of low-frequency fields. This was con-

firmed by use of a pickup coil and detecting 60 Hz fluctuations. The minimum suppression measured for the shield alone was > 20 dB parallel to the $\hat{z}$ axis of the trap, and the direction of the largest access opening in the shield. Shielding in excess of 60 dB at 60 Hz was measured in transverse directions.

The 1.3×10^{-3} T quantization field is oriented $45°$ with respect to the vacuum envelope axis. Initial measurements identified current instability due to power-supply ripple as dominating measured decoherence once the shield was installed. We implemented a custom current-regulation system based on a proportional-integral-differential feedback circuit, a series current-sense resistor, and a low-current field-effect transistor. To minimize the effect of thermal drifts in the electronic circuit on magnetic field stability, we selected special low-TC (thermal coefficient) components and temperature-stabilized the enclosure. The most critical components were the gain and sense resistors; these were selected to be low-TC metal foil resistors with less than 2 ppm/K and less than 3 ppm/K stability, respectively. A four-terminal current-sense resistor was selected with high-power-handling construction ($0.1 \, \Omega$ for the main coil and $0.25 \, \Omega$ for the transverse shim coils). Similar care was taken to select low-TC difference amplifiers for the input stage and a low-TC voltage reference. All sense and feedback components were thermally sunk to an Al enclosure that was thermally stabilized by use of Peltier coolers and a commercial temperature controller with milliKelvin stability. Stabilization reduced current ripple from ~ 1 mA to $\sim 30 \, \mu$A on the main field-coil current of 1.2 A. Net magnetic field fluctuations due to current ripple at the location of the ions were ~ 26 nT.

Measurements of the dephasing time including both the magnetic shield and the stabilization circuitry demonstrated extension of the qubit coherence to 1.41 ± 0.09 ms, more than $15\times$ longer than that without shielding and current stabilization, and sufficient for multiple transports before the qubit dephased. A spin-echo pulse doubles the coherence time to 2.99 ± 0.04 ms, indicating that slow shot-to-shot field fluctuations are small, and that decoherence is dominated by fluctuations on a millisecond time scale.

VII. MODE ENERGY EXCHANGE

The secular modes of the ions were constrained to change throughout the transports, both in frequency and orientation. For most parts of the transport, the splittings between the mode frequencies were sufficiently large and the transport speed was sufficiently slow that modes changed adiabatically and energy did not transfer between modes. However, at $\mathcal{C}$, the two principle axes that lie in the (x, z) plane were designed to have nearly degenerate secular frequencies ($\omega_x' \approx \omega_z' \approx 2\pi \times 5.7$ MHz), which could lead to mode-mixing. The third mode along $\hat{y}$ had a significantly higher frequency

$\omega_y' = 2\pi \times 11.3$ MHz, and would remain decoupled from the x and z modes. Since the radial modes were only Doppler laser-cooled before transport, x/z mode mixing would increase the excitation of the axial mode during transport. We employed two approaches that would minimize such axial excitation. First, the duration during which the ion was at $\mathcal{C}$ could be adjusted such to minimize the energy transfer between modes (by using a duration that corresponded to a full cycle of the mixing process). Alternately, a potential could be applied to various electrodes, which we will call the shim potential, to sufficiently break the degeneracy (in practice, $|\omega_x' - \omega_z'| > 2\pi \times 400$ kHz could be achieved) and suppress the mixing. Both methods were effective and yielded similar transport excitation, though the second approach was used for the results in Tables ?? and II.

However, in separate experiments, we explored a method for controlling energy transfer between the motional modes of a single ion by using field shims near the junction to tune ω_x' and ω_z' to near-degeneracy. Ideally, a demonstration of the method would work as follows. Prior to transport from $\mathcal{E}$, the ion is cooled to the axial ground state $|n_z = 0\rangle$ along $\hat{z}$ and prepared in Doppler-cooled thermal states in the transverse modes. If the relative orientation of the modes remains stationary as the ion approaches $\mathcal{C}$, the modes should not exchange energy, even if they become degenerate. However, if the x and z mode directions diabatically (fast compared to $1/\Delta\omega$) rotate $45°$ to new directions given by $x' = (x+z)/\sqrt{2}$ and $z' = (x-z)/\sqrt{2}$, we would expect the initial x oscillation to project onto the new mode basis with half of the energy going into each of the new modes. If $\Delta\omega' \equiv \omega_x' - \omega_z' \neq 0$, the two oscillations would then begin acquiring a relative phase $\phi = \Delta\omega' t$, where t is the period spent at $\mathcal{C}$. By then quickly transporting away from $\mathcal{C}$ towards $\mathcal{E}$ such that the mode axes rotate diabatically by $-45°$ back to their original orientation, the oscillations would project back onto the original oscillator basis. If the wait period is such that $\phi = \pi \times M$ (where M is an integer), the motion originally in the x mode would project back into the same mode. If, however, $\phi = \frac{\pi}{2} \times (2M - 1)$, then the x-motion would project into the z mode; that is, the energy would exchange between x and z modes.

We demonstrated the basic features of this exchange as follows. To tune the ω_x' and ω_z' close to degeneracy, an external shim potential with an adjustable amplitude was applied. The shim potential consisted of various contributions from 17 control electrodes near $\mathcal{C}$, each multiplied by the overall scaling factor A. These contributions were selected so that the net shim potential would primarily alter the frequency splitting without significantly affecting other trapping parameters (such as the position of the trapping minimum and the y mode frequency).

The black trace in Fig. 13(a) shows $\bar{n}_z$ for the axial mode after $\mathcal{E}$-$\mathcal{C}$-$\mathcal{E}$ transport, as the wait period at $\mathcal{C}$ was varied. We derive $\bar{n}_z$ from sideband measurements, as described above, and assume a thermal distribution. Although this assumption may not be strictly valid, it
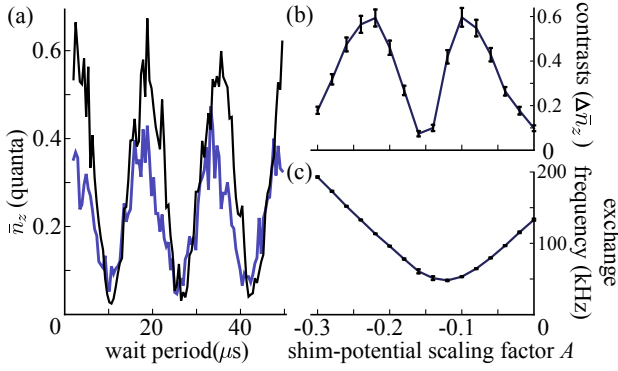
FIG. 13: (a) Average motional excitation ($\bar{n}_z$) in the axial mode after an $\mathcal{E}$-$\mathcal{C}$-$\mathcal{E}$ transport, versus the duration at $\mathcal{C}$ (wait period). The black trace indicates exchange of energy between the z mode, prepared near the ground state (at $\mathcal{E}$), and the x mode, prepared in a thermal state via Doppler cooling. The smaller blue trace represents the identical preparation, except the transport was performed twice. During the first transport, the wait period was set to maximize the energy transfer from the radial mode to the axial mode, followed by returning the ion to $\mathcal{E}$. After re-cooling the axial mode to the ground state, the round-trip transfer was repeated. The contrast was decreased (blue trace), indicating that less transverse mode energy was available for transfer to the z mode and therefore indicating cooling of the x mode. (b) and (c) The exchange contrast and exchange frequency (respectively), plotted versus the shim-potential scaling factor A.

should give a reasonable approximation for $\bar{n}_z < 1$. Oscillations between an excited and near-ground state energy are visible. The projection process began prior to the ion reaching $\mathcal{C}$ and transport was too slow for the projection to be perfectly diabatic. Thus, the phase of the exchange oscillation in Fig. 13(a) is not well determined and was observed to depend on both the exchange frequency and the details of the approach to $\mathcal{C}$ (including speed and trajectory). In practice, it was difficult to maintain a constant phase for more than a few minutes, as drifts in the potential, likely caused by transient charge buildup and dissipation on the electrodes and also pseudopotential amplitude changes, caused the exchange frequency to drift over that time scale.

Figure 13(b) displays the oscillation contrast $\Delta\bar{n}_z = \max(\bar{n}_z) - \min(\bar{n}_z)$ for various scaling factors, A, of the shim potential, while Fig. 13(c) gives the frequency of those oscillations versus the shim scaling factor. In separate experiments, the two mode frequencies at $\mathcal{C}$ were measured as a function of A by driving excitations with an oscillatory potential applied to the control electrodes. The difference between the two mode frequencies, $\Delta\omega' = |\omega'_x - \omega'_z|$, was observed to match the oscillation frequency of the exchange process. Figure 13(c) suggests $\Delta\omega'$ is high on the extreme ends of the A range, while Fig. 13(b) shows a reduction in contrast in these regions of high $\Delta\omega'$, likely due to the reduction in diabaticity when $\Delta\omega'$ was large. This conclusion was supported by the observation that the contrast decreased as the ion

transport speed was reduced. However, there was a maximum speed, above which contrast no longer increased, because other sources of excitation began to obscure the oscillatory signal.

From Fig. 13(b), we see that the fringe contrast was also minimized for shim scaling factors near $A = -0.15$, where $\Delta\omega'$ was small. This reduction in contrast can be explained as coinciding with the condition where the initial mode orientation is identical to the rotated mode orientation and thus the modes do not mix when projected, which is a condition not necessarily related to $\Delta\omega'$. (We note that the A value for minimum exchange frequency does not match that for minimum contrast.) Unfortunately, it was not possible to verify this, as we could not measure the mode orientation at $\mathcal{C}$, due to lack of laser-beam access.

In the case where the energy from the x mode was transferred into the z mode, the ion could be returned to $\mathcal{E}$ for a second round of ground-state cooling of the z mode. In the experiment, the exchange process in $\mathcal{C}$ was repeated and the results are shown as the blue trace in Fig. 13(a), where a noticeable decrease in the ion's axial excitation was observed compared to the first experiment without the second stage of cooling. The small relative phase shift for the two traces in Fig. 13(a) was due to the slow drift of $\Delta\omega'$ over the several minutes required to take the two traces.

Ideally, all of the energy would be transferred from the x mode into the z mode, and the subsequent cooling of the z mode would leave both modes in the ground state, leading to no oscillation during the second trip into $\mathcal{C}$. In practice, complete transfer was inhibited for two primary reasons. First, the ions were not being transported fast enough to make a clean diabatic projection of the motion onto the switched axes. Second, for complete energy transfer, the projection should be onto axes rotated by $\pm 45°$. Any other angles would have resulted in incomplete transfer of energy. Attempts were made to adjust additional shims in hopes of realizing configurations closer to $\pm 45°$. However, as $\Delta\omega' \to 0$, it, again, becomes difficult to predict the mode orientation with our idealized computer models and we could not experimentally determine the mode axes in $\mathcal{C}$.

Nevertheless, we observed a clear and easily reproducible reduction in maximum oscillation amplitude (Fig. 13(a)) from $\max(\bar{n}_z) = 0.68 \pm 0.08$ to $\max(\bar{n}_z) = 0.40 \pm 0.05$ after the second round of cooling, indicating the radial mode energy was being reduced. The use of additional rounds of exchange followed by cooling reduced $\max(\bar{n}_z)$ further, but after three or four exchange rounds, other sources of excitation offset the energy reduction.

When optimized, this technique might be used to cool all modes of a single ion to the ground state, while having the ability only to ground-state cool a single mode, as for the laser beam configuration used here. A junction is not required; all that is needed is a trap that can diabatically change the relevant mode orientations by $\pm 45°$, which could be possible in many trap configurations.

VIII. CONCLUSION

In conclusion, we have demonstrated that transport through a two-dimensional trap array incorporating a junction can be highly reliable and excite an ion's motion by less than one quantum. This is a significant improvement over prior work with junction arrays [1, 18] and suggests the viability of trap arrays incorporating junctions for use in large-scale ion-based quantum information processing. In addition, we have implemented a mu-metal shield and current stabilization to reduce qubit decoherence. We have also examined a technique for transferring energy between motional modes.

DAC-update noise can be mitigated with the use of more appropriate filters such as the Butterworth filters used here and/or faster DAC update rates. Noise on the trapping rf potential can result in motional excitation at pseudopotential barriers as described in Sec. V A. The junction design criteria in Ref. [19] included minimizing these barriers. However, the results here show that the slope of the pseudopotential barrier is more important than the barrier height for suppressing motional excitation, suggesting that suppression of barrier height may not be a necessary constraint in future designs. Also, as observed here, with proper rf filtering, significant barrier slopes can be tolerated without causing significant heating.

The technique for determining the waveforms described in this report can be extended to incorporate multiple trapping wells by expanding Eq. (9) to include multiple minima. Transport procedures such as the ion exchange in Ref. [17] are also amenable to these solving techniques. Separating and combining of trapping wells requires consideration of the potential's quartic term [43]. Therefore, $\mathcal{P}$ in Eq. (8) could be expanded to include fourth-order derivatives.

With the use of multiple junctions, the techniques described here could help provide a path toward transfer of information in a large-scale ion-based quantum processor and enable an increased number of qubits in quantum algorithm experiments. To do this, waveforms must be expanded to incorporate many trapping wells. Also, it is likely that a sympathetic cooling ion species will need to be co-trapped with the qubit ions to allow removal of the motional excitation from electronic noise, multiple junction transports, and separating and re-combining wells [15, 21, 44]. If sympathetic-cooling ions are present, it may be advantageous to transport both ion species through a junction in a single local trapping well. Since the pseudopotential (and micromotion) are mass dependent, the qubit and cooling ions will experience different potentials, which could lead to additional motional excitation. If such excitation is excessive, it should still be possible to separate the ions into individual wells by species and pass the different species through junctions separately, followed by recombination.

[1] R.B. Blakestad, C. Ospelkaus, A.P. VanDevender, J.M. Amini, J. Britton, D. Leibfried, and D.J. Wineland, Phys. Rev. Lett. **102**, 153002 (2009).

[2] R. Blatt and D.J. Wineland, Nature **453**, 1008 (2008).

[3] C. Monroe and M.D. Lukin, Physics World **21**, 32 (2008).

[4] H. Häffner, C.F. Roos, and R. Blatt, Phys. Rep. **469**, 155 (2008).

[5] J.I. Cirac and P. Zoller, Nature **404**, 579 (2000).

[6] D.J. Wineland, C. Monroe, W.M. Itano, D. Leibfried, B.E. King, and D.M. Meekhof, J. Res. Natl. Inst. Stand. Technol. **103**, 259 (1998).

[7] D. Kielpinski, C. Monroe, and D.J. Wineland, Nature **417**, 709 (2002).

[8] L.-M. Duan and C. Monroe, Rev. Mod. Phys. **82**, 1209 (2010).

[9] G.-D. Lin, S.-L. Zhu, R. Islam, K. Kim, M.-S. Chang, S. Korenblit, C. Monroe, and L.-M. Duan, Euro. Phys. Lett. **86**, 60004 (2009).

[10] J.I. Cirac and P. Zoller, Phys. Rev. Lett. **74**, 4091 (1995).

[11] R.J. Hughes, D.F.V. James, E.H. Knill, R. Laflamme, and A.G. Petschek, Phys. Rev. Lett. **77**, 3240 (1996).

[12] M.A. Rowe, A. Ben-Kish, B. Demarco, D. Leibfried, V. Meyer, J. Beall, J. Britton, J. Hughes, W.M. Itano, B. Jelenkovic, C. Langer, T. Rosenband, and D.J. Wineland, Quant. Inf. Comput. **2**, 257 (2002).

[13] M.D. Barrett, J. Chiaverini, T. Schaetz, J. Britton, W.M. Itano, J.D. Jost, E. Knill, C. Langer, D. Leibfried, R. Ozeri, and D.J. Wineland, Nature **429**, 737 (2004).

[14] G. Huber, T. Deuschle, W. Schnitzler, R. Reichle, K. Singer, and F. Schmidt-Kaler, New J. Phys. **10**, 013004 (2008).

[15] J.P. Home, D. Hanneke, J.D. Jost, J.M. Amini, D. Leibfried, and D.J. Wineland, Science **325**, 1227 (2009).

[16] J.F. Eble, S. Ulm, P. Zahariev, F. Schmidt-Kaler, and K. Singer, J. Opt. Soc. Am. **27**, A99 (2010).

[17] F. Splatt, M. Harlander, M. Brownnutt, F. Zähringer, R. Blatt, and W. Hänsel, New J. Phys. **11**, 103008 (2009).

[18] W.K. Hensinger, S. Olmschenk, D. Stick, D. Hucul, M. Yeo, M. Acton, L. Deslauriers, C. Monroe, and J. Rabchuk, Appl. Phys. Lett. **88**, 034101 (2006).

[19] J.M. Amini, H. Uys, J.H. Wesenberg, S. Seidelin, J. Britton, J.J. Bollinger, D. Leibfried, C. Ospelkaus, A.P. VanDevender, and D.J. Wineland, New J. Phys. **12**, 033031 (2010).

[20] D.L. Moehring, C. Highstrete, M.G. Blain, K. Fortier, R. Halti, D. Stick, and C. Tigges, arXiv:1105.1834 (2011).

[21] J.D. Jost, Ph.D. thesis, University of Colorado (2010).

[22] J. Chiaverini, R.B. Blakestad, J. Britton, J.D. Jost, C. Langer, D. Leibfried, R. Ozeri, and D.J. Wineland,

Quant. Inf. Comput. **5**, 419 (2005).

[23] J.H. Wesenberg, Phys. Rev. A **79**, 013416 (2009).

[24] M.N.O. Sadiku, *Numerical Techniques in Electromagnetics* (CRC Press, Boca Raton, 2009), 3rd ed.

[25] K. Singer, U. Poschinger, M. Murphy, P. Ivanov, F. Ziesel, T. Calarco, and F. Schmidt-Kaler, Rev. Mod. Phys. **82**, 2609 (2010).

[26] R.B. Blakestad, Ph.D. thesis, University of Colorado (2010).

[27] P.E. Gill, W. Murray, and M.H. Wright, *Practical Optimization* (Academic Press, London, 1981).

[28] H. Uys, private communication.

[29] R. Reichle, D. Leibfried, R.B. Blakestad, J. Britton, J.D. Jost, E. Knill, C. Langer, R. Ozeri, S. Seidelin, and D.J. Wineland, Fortschr. Physik **54**, 666 (2006).

[30] D. Hucul, M. Yeo, S. Olmschenk, C. Monroe, W.K. Hensinger, and J. Rabchuk, Quant. Inf. Comput. **8**, 501 (2008).

[31] C. Monroe, D.M. Meekhof, B.E. King, S.R. Jefferts, W.M. Itano, D.J. Wineland, and P. Gould, Phys. Rev. Lett. **75**, 4011 (1995).

[32] Q.A. Turchette, D. Kielpinski, B.E. King, D. Leibfried, D.M. Meekhof, C.J. Myatt, M.A. Rowe, C.A. Sackett, C.S. Wood, W.M. Itano, C. Monroe, and D.J. Wineland, Phys. Rev. A **61**, 063418 (2000).

[33] H. Walther, Adv. At. Mol. Phys. **31**, 137 (1993).

[34] S.R. Jefferts, C. Monroe, E.W. Bell, and D.J. Wineland, Phys. Rev. A **51**, 3112 (1995).

[35] U. Tietze and Ch. Schenk, *Electronic Circuits: Handbook for Design and Applications* (Springer, Berlin, 2008).

[36] L. Deslauriers, P.C. Haijan, P.J. Lee, K.A. Brickman, B.B. Blinov, M.J. Madsen, and C. Monroe, Phys. Rev. A **70**, 043408 (2004).

[37] R.J. Epstein, S. Seidelin, D. Leibfried, J.H. Wesenberg, J.J. Bollinger, J.M. Amini, R.B. Blakestad, J. Britton, J.P. Home, W.M. Itano, J.D. Jost, E. Knill, C. Langer, R. Ozeri, N. Shiga, and D.J. Wineland, Phys. Rev. A **76**, 033411 (2007).

[38] N. Daniilidis, S. Narayanan, S.A. Møller, R. Clark, T.E. Lee, P.J. Leek, A. Wallraff, St. Schulz, F. Schmidt-Kaler, and H. Häffner, New J. Physics **13**, 013032 (2011).

[39] C. Langer, R. Ozeri, J.D. Jost, J. Chiaverini, B. De-Marco, A. Ben-Kish, R.B. Blakestad, J. Britton, D.B. Hume, W.M. Itano, D. Leibfried, R. Reichle, T. Rosenband, T. Schaetz, P.O. Schmidt, and D.J. Wineland, Phys. Rev. Lett. **95** (2005).

[40] K. Mølmer and A. Sørensen, Phys. Rev. Lett. **82**, 1835 (1999).

[41] D. Leibfried, B. DeMarco, V. Meyer, D. Lucas, M. Barrett, J. Britton, W.M. Itano, B. Jelenkovic, C. Langer, T. Rosenband, and D.J. Wineland, Nature **422**, 412 (2003).

[42] P.J. Lee, K.-A. Brickman, L. Deslauriers, P.C. Haljan, L.-M. Duan, and C. Monroe, J. Opt. B: Quantum Semiclass Opt. **7**, S371 (2005).

[43] J.P. Home and A.M. Steane, Quant. Inf. Comput. **6**, 289 (2006).

[44] D. Hanneke, J.P. Home, J.D. Jost, J.M. Amini, D. Leibfried, and D.J. Wineland, Nature Phys. **6**, 13 (2009).

[45] For the 0.999995 success probability figure, we only verified that each transport successfully returned the ion to $\mathcal{E}$, not whether the ion successfully moved the ion through the junction. Given the low rates of motional excitation, and the fact that we did verify that the ions move through the junction using 10,000 experiments, it is reasonable to assume the ion did travel through the junction if the ion successfully returned to $\mathcal{E}$.